ARTICLE

Open Access

Material-specific high-resolution table-top extreme ultraviolet microscopy

Wilhelm Eschen[1,2✉], Lars Loetgering[1,2,3], Vittoria Schuster[1,2], Robert Klas[1,2], Alexander Kirsche[1,2], Lutz Berthold[4], Michael Steinert[1], Thomas Pertsch[1,5], Herbert Gross[1], Michael Krause[4], Jens Limpert[1,2,5] and Jan Rothhardt[1,2,5]

Abstract
Microscopy with extreme ultraviolet (EUV) radiation holds promise for high-resolution imaging with excellent material contrast, due to the short wavelength and numerous element-specific absorption edges available in this spectral range. At the same time, EUV radiation has significantly larger penetration depths than electrons. It thus enables a nano-scale view into complex three-dimensional structures that are important for material science, semiconductor metrology, and next-generation nano-devices. Here, we present high-resolution and material-specific microscopy at 13.5 nm wavelength. We combine a highly stable, high photon-flux, table-top EUV source with an interferometrically stabilized ptychography setup. By utilizing structured EUV illumination, we overcome the limitations of conventional EUV focusing optics and demonstrate high-resolution microscopy at a half-pitch lateral resolution of 16 nm. Moreover, we propose mixed-state orthogonal probe relaxation ptychography, enabling robust phase-contrast imaging over wide fields of view and long acquisition times. In this way, the complex transmission of an integrated circuit is precisely reconstructed, allowing for the classification of the material composition of mesoscopic semiconductor systems.

Introduction

Advances in nano-scale metrology of silicon-based devices are crucial for progress in diverse fields, with applications spanning from semiconductor miniaturization[1], energy conversion, and storage, such as next-generation solar cells[2] and battery materials[3], to nanostructures with advanced optical functionality, like metamaterials[4] and photonic circuits[5]. The extreme ultraviolet lithography (EUVL) node at 13.5 nm wavelength was selected as a reasoned choice. The electronic structure of tin plasmas provides prominent emission peaks at 13.5 nm wavelength[6,7], while multilayer mirrors such as Mo/Si and Mo/Be reach reflectivities of up to 70%[8,9]. Moreover, at 13.5 nm the penetration depth of EUV photons in silicon is orders of magnitude higher than many elements across the periodic table. Likewise, in comparison to electrons, EUV photons can shed light into the interior of silicon-based environments. The electromagnetic region below the silicon L edge is therefore referred to as the *silicon transparency window*—an ideal testbed for silicon-based substrates and functional materials.

In the past decade, imaging at EUV wavelengths has undergone a transformation. Imaging techniques have successfully been transferred from large-scale facilities[10], such as synchrotrons and free-electron lasers, to laboratory-scale sources such as soft X-ray lasers[11−13] and laser-plasmas[14]. Recently, EUV sources driven by high-harmonic generation (HHG)[15−17] have experienced tremendous progress, which resulted in increased photon flux and stability. These highly coherent EUV sources have shown promising results using lensless imaging[18−20]. In particular, the emergence of ptychography[21,22] has offered a solution to some of the main problems encountered with EUV radiation: its lensless operation principle avoids absorptive losses, aberrations induced by the image forming optics, and its ability to

Correspondence: Wilhelm Eschen (wilhelm.eschen@uni-jena.de)
[1]Institute of Applied Physics, Abbe Center of Photonics, Friedrich-Schiller-Universität Jena, Albert-Einstein-Str. 15, 07745 Jena, Germany
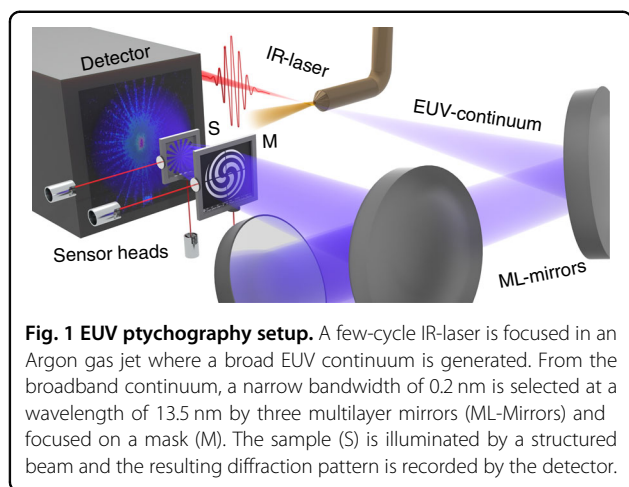[2]Helmholtz-Institute Jena, Fröbelstieg 3, 07743 Jena, Germany
Full list of author information is available at the end of the article

Fig. 1 EUV ptychography setup. A few-cycle IR-laser is focused in an Argon gas jet where a broad EUV continuum is generated. From the broadband continuum, a narrow bandwidth of 0.2 nm is selected at a wavelength of 13.5 nm by three multilayer mirrors (ML-Mirrors) and focused on a mask (M). The sample (S) is illuminated by a structured beam and the resulting diffraction pattern is recorded by the detector.

perform wavefront sensing enables the deconvolution of illumination-induced aberrations, resulting in quantitative phase imaging (QPI). These capabilities are afforded by data-driven techniques. A sequence of diffraction patterns is collected on a pixelated detector while the specimen is laterally translated through a focused beam (compare Fig. 1). The scan points are chosen in such a way that diffraction patterns from adjacent positions contain overlapping information. In this way, both the illumination wavefront and a phase-sensitive sample micrograph are jointly retrieved. Nevertheless, ptychography with table-top HHG sources[23] is arguably in its infancy. Despite recent highlights in EUV ptychography, such as sub-wavelength resolution on periodic samples[24], bioimaging of hippocampal neurons[25] as well as phase-sensitive reflectometry[26], additional element-specificity is needed to meet the demands from the semiconductor industry and harness the prominent contrast mechanisms in silicon-based environments.

In this work, we present an actively stabilized, high-resolution, quantitative EUV transmission microscope operating in the silicon transparency window. We demonstrate wavelength-scale resolution combined with material-specific imaging. A critical ingredient is the use of structured illumination to overcome the limitations of conventional EUV focusing optics. To this end, an amplitude mask is placed in front of the sample, which shapes the illuminating probe beam. As an algorithmic novelty, we propose orthogonal probe relaxation (OPR)[27] combined with multiple mixed-states (m-s)[28], which results in a precise reconstruction of the specimen's scattering amplitude. Combining the stabilized setup with the structured illumination, we achieve a diffraction-limited half-pitch resolution of 16 nm on a high-contrast, non-periodic sample. In addition, a thin lamella of a silicon-based integrated circuit, extracted from a solid-state disc, is investigated. For the first time, the material

composition is retrieved by a single EUV ptychography scan over a wide field of view utilizing the reconstructed scattering amplitude. We believe the current work is an important step forward toward the integration of high-resolution metrology into the realm of EUVL as well as toward material-specific inspection of functional materials in silicon-based environments.

Results

Experimental setup

Ultrashort fiber laser systems enable average powers in the kilowatt range with millijoule pulse energies[29]. HHG sources operated by these lasers provide high photon flux reaching the milliwatt range for low photon energies[17]. Here, a high-power few-cycle laser is focused into an argon gas jet (see Fig. 1). The short (<10 fs) IR driving laser pulses generate a broadband EUV continuum via HHG, which yields a photon flux of 7×10^9 ph/s/eV at 92 eV with particularly high power and pointing stability. More details on the HHG source can be found in the "Materials and methods" section. The EUV radiation is directed and focused onto the sample by means of three multilayer mirrors, which are used to select a central wavelength of 13.5 nm (92 eV) within a 0.2 nm bandwidth (FWHM) window of the broadband continuum. The cascade of three mirrors has been designed to fully compensate for astigmatism induced by the spherical mirrors. The resulting EUV focal spot was characterized by ptychography and exhibits an intensity full-width half-maximum of 3.8 μm and 2.6 μm, which is significantly smaller than in previous two-mirror configurations[30]. More details about the out-of-plane setup and the beam characterization can be found in the supplement. The monochrome EUV beam is directed onto an amplitude mask placed directly in front of the sample. The mask allows for structuring the illumination. Ptychography relies on the precise knowledge of the probe beam with respect to the object at each scan position. Moreover, unaccounted position drifts during the acquisition of a diffraction pattern lead to unwanted decoherence effects[31] and model mismatch[27]. To ensure stable and reliable positioning over hours of measurement time, both the sample and mask holder position are tracked by a laser interferometer and actively stabilized via a feedback loop. Diffraction patterns are recorded by a CCD which is placed 30 mm behind the sample resulting in a detection numerical aperture (NA) of 0.42. Finally, the probe beam and the object are computationally reconstructed by means of ptychographic algorithms[21,22], which are detailed in the "Materials and methods" section.

EUV ptychography using structured light

In recent years, structured illumination has turned out to be beneficial for ptychography for multiple reasons.

First, a larger spatial frequency spectrum increases the spread of the diffraction pattern on the detector. The zeroth order of the diffraction is, therefore, less intense and leads to relaxed dynamic range requirements on the detector[32]. Second, the broadened spatial frequency spectrum increases the diffraction-limited resolution[33]. Third, a structured beam improves the convergence of the reconstruction algorithms. Due to the fine structures of the beam, a translation of the probe leads to more diverse diffraction patterns, which results in stronger information[34]. So far structured illumination has been used for experiments in the visible[32], soft[35], and hard X-ray[33,34] range. In table-top EUV ptychography multilayer mirrors with relatively low numerical apertures are the prevailing method of choice[23,30,36]. Structured and focused EUV beams have so far only been achieved with a specialized Fresnel zone plate[37], which are, however, limited in

photon efficiency and require additional optical components for spectral selection.

In this work, we shape a structured beam by placing an absorbing nano-structured mask with a fill factor of 50% at roughly 200 μm upstream of the sample. The combination of multilayer mirrors and the amplitude mask enables a photon efficient spectral selection, structuring, and focusing of the EUV probe beam. Below, we demonstrate that such dedicated illumination engineering pays off by drastically improving the reconstruction quality and lateral resolution.

To investigate the influence of a structured illumination on the EUV image quality, two independent measurements were performed using a smooth (unstructured) and a structured illumination, respectively. A pinhole with a diameter of 8 μm is used to restrict the size of the smooth (unstructured) beam. The ptychographic reconstruction of the object is shown in Fig. 2a. The colored insets (red,
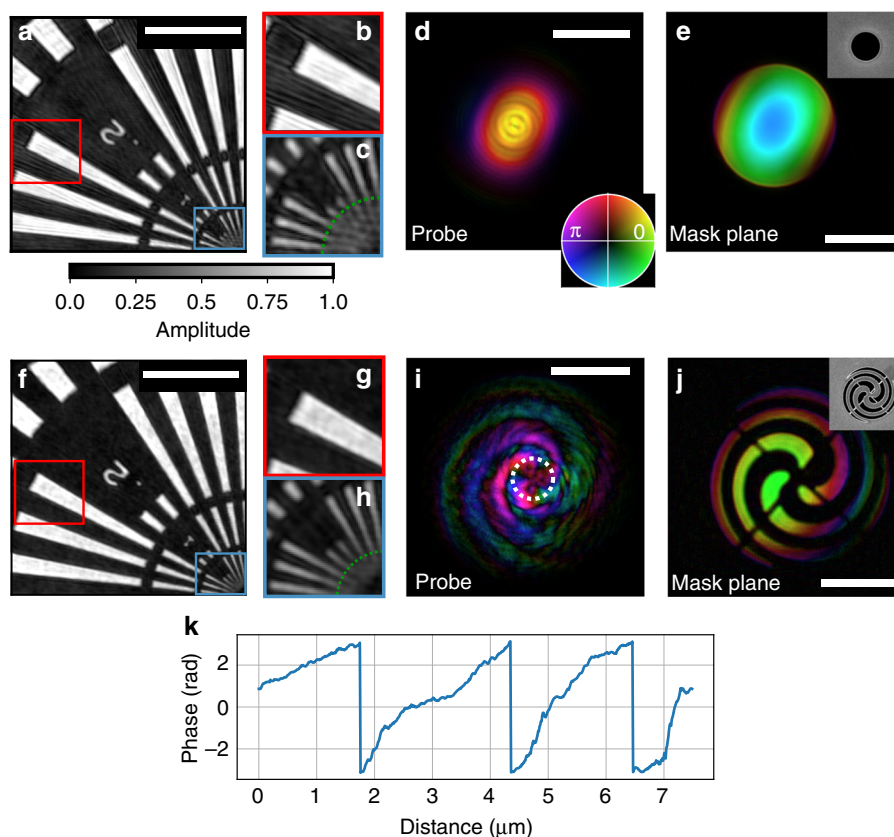

Fig. 2 EUV ptychography using structured beams. a Reconstructed transmissivity of the Siemens star using an unstructured illumination. The reconstruction exhibits spurious mid-spatial-frequency modulations, which are displayed in inset (**b**). A magnified view of the center of the Siemens star is shown in (**c**). The corresponding reconstructed probe is shown in (**d**). **e** The probe back-propagated into the mask plane. The small inset in (**e**) shows an SEM image of the mask, which is a 8 μm diameter pinhole. **f** Reconstructed transmission of the Siemens star using structured light showing fewer modulations in (**g**) and a higher resolution in (**h**) as compared to the unstructured reconstruction (**b**, **c**). The green circular line in (**c**), **h** corresponds to the smallest radius where the spokes are still resolved. **i**, **j** Reconstructed illumination in the sample and mask plane. The small inset in (**j**) shows the SEM image of the mask for comparison. **k** Azimuthal lineout of the probe phase along the white, dotted path indicated in (**i**). The scale bar in (**a**), **f** indicates 2 μm and the scale bar of (**d**), **e**, **i**, **j** corresponds to 5 μm. The brightness and hue of (**d**), **e**, **i**, **j** encode modulus and phase, respectively.

blue) highlight regions where we identified spurious modulations in the reconstructed micrograph (Fig. 2b). Clearly, these are not real features of the object but imaging artifacts that hinder quantitative imaging. The distorted image quality can be attributed to the low translation diversity of the unstructured probe beam[34], which is shown in Fig. 2d. The back-propagated complex electric field inside the mask aperture (Fig. 2e) matches with the scanning electron microscopy (SEM) image of the fabricated pinhole (small inset). In the mask plane, a slight phase curvature is visible, which is due to the out-of-focus position of the mask.
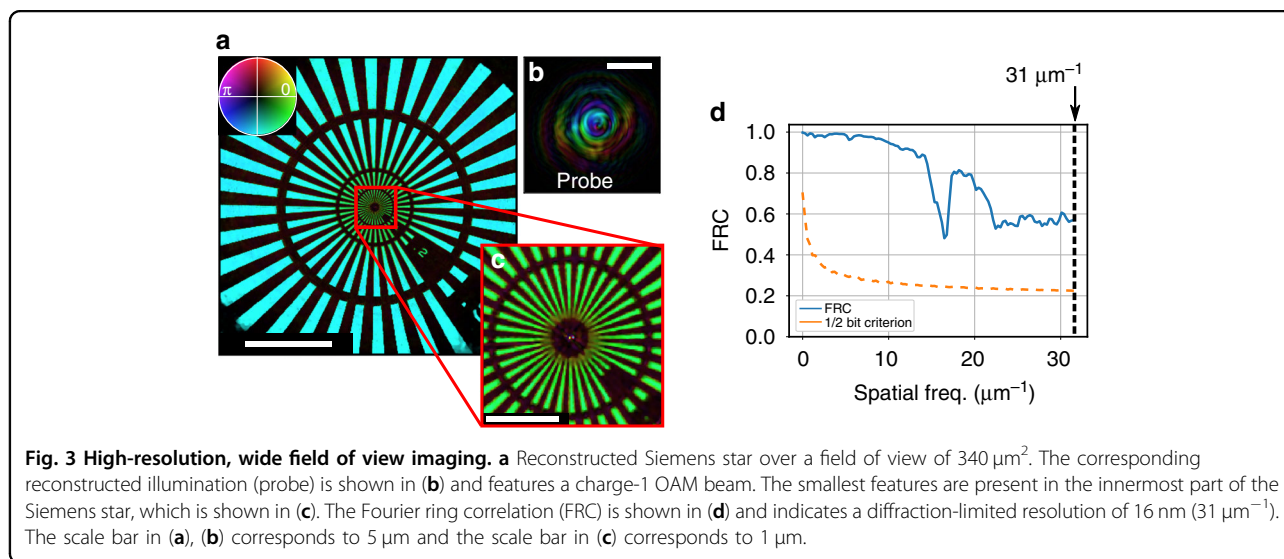
In the next step, a mask that results in a highly structured beam on the sample is used. The exposure time was doubled to keep the overall number of detected photons per diffraction pattern comparable to the previous experiment using an unstructured pinhole. The resulting reconstruction of the object is displayed in Fig. 2f. We observe an overall improved image quality, which is due to a reduction of spurious modulation as compared to the reconstruction obtained from the unstructured beam. By direct comparison of the blue insets in Fig. 2a, f, we find that a higher resolution is achieved by means of the structured beam. While for the unstructured beam spokes down to a size of 53 nm are resolved, for the highly structured beam features down to a size of 43 nm are resolved (compare enlarged innermost spokes in Fig. 2c, h). The reconstructed structured beam in the sample plane, which is shown in Fig. 2i, was achieved by nanopatterning the mask with a spiral shape[38]. The illumination back-propagated into the mask plane shows the spiral mask (Fig. 2j), which matches well with the corresponding SEM images in the inset.
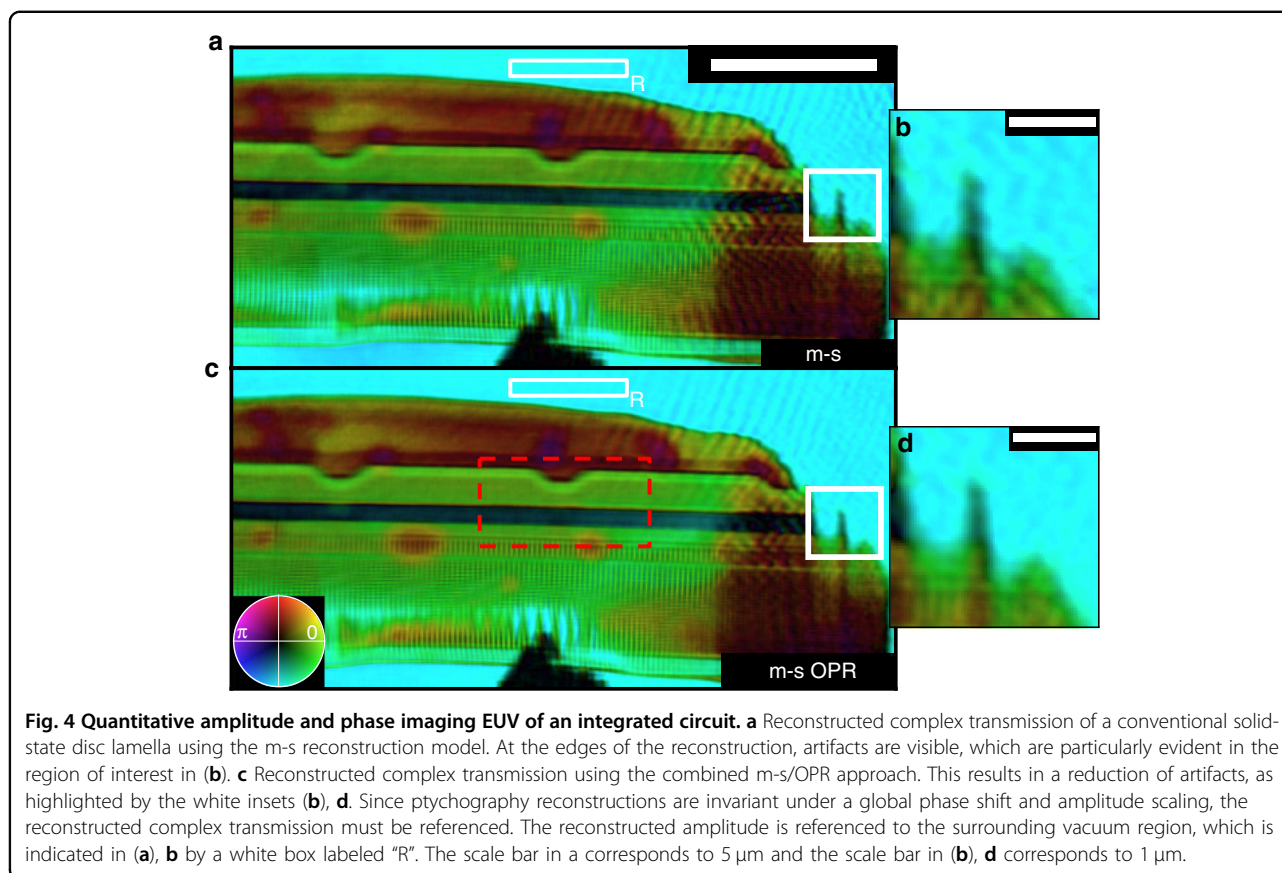
The spiral-shaped pattern is a small version of a spiral Fresnel zone plate and was used here for multiple reasons.

First, the pattern leads to an enriched spatial frequency content in the illumination. Second, in comparison to simpler structures, such as gratings, the spiral masks feature beam structuring in various directions. Third, the generation of twisted beams with a table-top source could open up new avenues toward OAM-induced magnetic dichroism microscopy, as recently demonstrated at a free-electron laser[39]. In this experiment, a charge 3 orbital angular momentum (OAM) was created. Figure 2k indicates an azimuthal lineout of the phase of the reconstructed wavefront along the white, dotted path in Fig. 2i, confirming the charge 3 OAM of the beam. Different types of OAM beams can be easily generated with the presented technique by adapting the beam shaping mask[40].

High-resolution, wide field-of-view ptychographic imaging at 13.5 nm

The combination of structured illumination and interferometric stability in the positioners allows for high-dynamic range (HDR) data acquisition over long-term scans. This enables both wide fields of view and high-resolution imaging. A Siemens star test pattern was scanned for 101 positions. For each position, two diffraction patterns with exposure times of 3 s and 45 s were recorded and stitched together into a single high-dynamic-range diffraction pattern. The time required for the acquisition of the entire scan (101 positions), including the movement of the positioners and read-out of the camera, was 91 min. The high-resolution reconstruction of the object is shown in Fig. 3a, resulting in a total field of view of 340 μm². The reconstructed probe is shown in Fig. 3b. To demonstrate the flexibility of our mask-based approach, here a charge-1 OAM beam was generated. The achieved high-resolution is shown in the innermost region

Fig. 3 High-resolution, wide field of view imaging. a Reconstructed Siemens star over a field of view of 340 μm². The corresponding reconstructed illumination (probe) is shown in (**b**) and features a charge-1 OAM beam. The smallest features are present in the innermost part of the Siemens star, which is shown in (**c**). The Fourier ring correlation (FRC) is shown in (**d**) and indicates a diffraction-limited resolution of 16 nm (31 μm⁻¹). The scale bar in (**a**), (**b**) corresponds to 5 μm and the scale bar in (**c**) corresponds to 1 μm.

Fig. 4 Quantitative amplitude and phase imaging EUV of an integrated circuit. a Reconstructed complex transmission of a conventional solid-state disc lamella using the m-s reconstruction model. At the edges of the reconstruction, artifacts are visible, which are particularly evident in the region of interest in (**b**). **c** Reconstructed complex transmission using the combined m-s/OPR approach. This results in a reduction of artifacts, as highlighted by the white insets (**b**), **d**. Since ptychography reconstructions are invariant under a global phase shift and amplitude scaling, the reconstructed complex transmission must be referenced. The reconstructed amplitude is referenced to the surrounding vacuum region, which is indicated in (**a**), **b** by a white box labeled "R". The scale bar in a corresponds to 5 μm and the scale bar in (**b**), **d** corresponds to 1 μm.
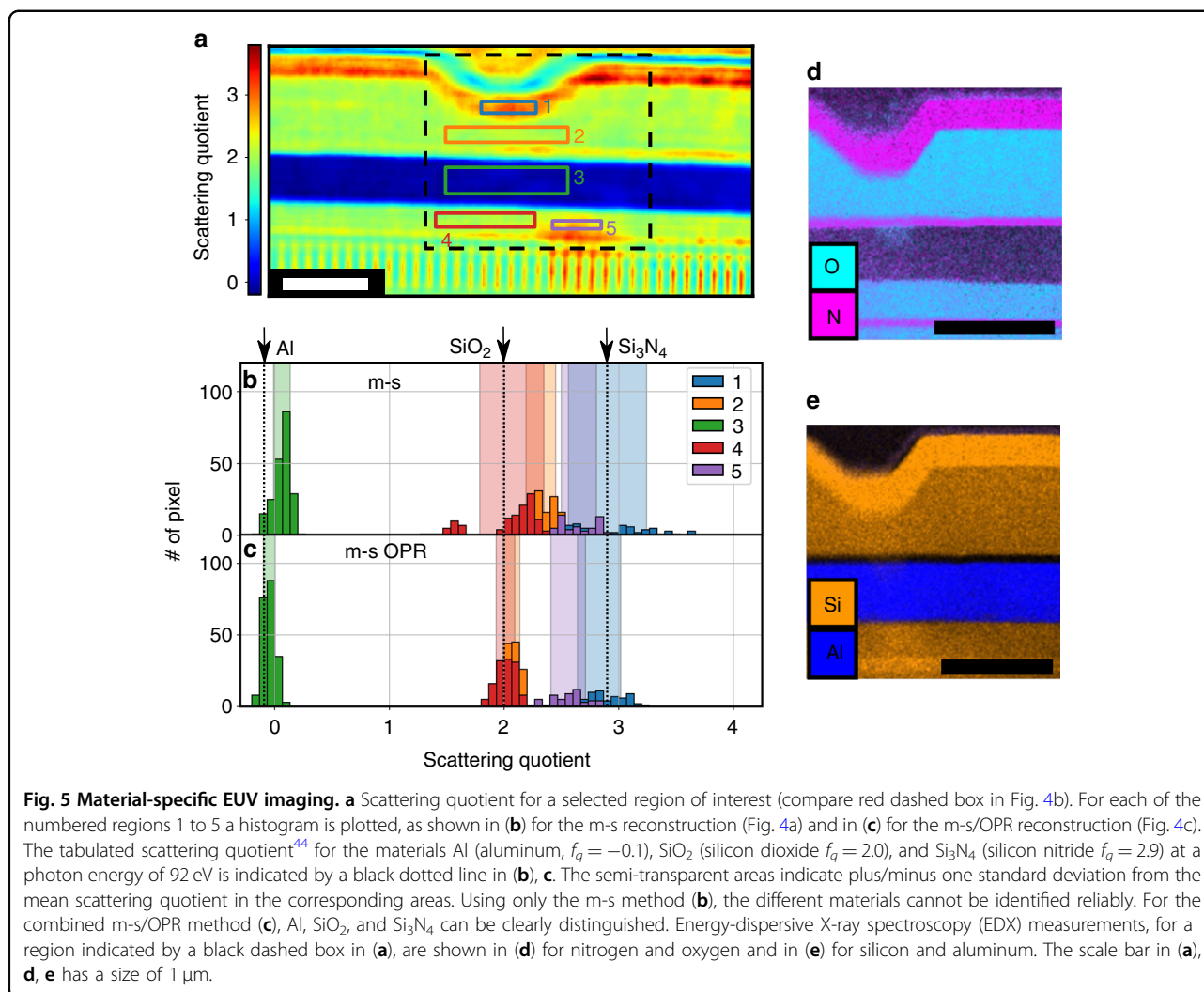
of the Siemens star, which contains the smallest features and is shown in Fig. 3c. The Fourier ring correlation (FRC), a widely used measure for the estimation of resolution in X-ray ptychography[41], was calculated and combined with the half-bit criterion[42]. To this end, a second, independent data set was acquired and the FRC was calculated from both reconstructions, the result of which is shown in Fig. 3d. The FRC curve does not intersect with the half-bit criterion up to the highest detected spatial frequency at the edge of the detector which corresponds to a spatial frequency of $31\,\mu m^{-1}$ and hence proves a diffraction-limited half-pitch resolution of 16 nm. Note that this resolution analysis is valid over the entire field of view. More details on the reconstruction can be found in the "Materials and methods" section.

Quantitative, material-specific EUV imaging of an integrated circuit

Integrated circuits are the foundation of modern computer technology. As the structures of these devices shrink, the characterization of integrated circuits and of the machines used to manufacture them is of great interest. Here, the strengths of ptychography at 92 eV are demonstrated using a highly integrated structure of a conventional solid-state disc (SSD). For this purpose, a

lamella of the SSD was extracted and placed in the EUV ptychography microscope. More details on the sample preparation can be found in the "Materials and methods" section.

The reconstructed complex transmission of the lamella is shown in Fig. 4a. At the bottom of the lamella, an opaque spot is visible, which can be attributed to contamination and was not visible during the preparation of the sample. In the center, the conducting and insulating structures of the SSD are visible. The reconstructed phase in this area shows a high contrast, which can be explained by numerous materials used for the fabrication and demonstrates the high sensitivity of EUV microscopy. Since the complex object transmission function of the object (i.e., transmissivity and phase shift) retrieved by ptychography contains both quantitative amplitude and phase information, the scattering quotient, averaged along the projection direction, can be accessed. This scattering quotient is independent of the thickness[43] and allows identifying different materials by comparison with measured complex refractive indices of different materials[44]. More details on the scattering quotient can be found in the "Materials and methods" section. To ensure a reliable material identification, the transmissivity and phase shift of the object needs to be reconstructed with high

Fig. 5 Material-specific EUV imaging. a Scattering quotient for a selected region of interest (compare red dashed box in Fig. 4b). For each of the numbered regions 1 to 5 a histogram is plotted, as shown in (**b**) for the m-s reconstruction (Fig. 4a) and in (**c**) for the m-s/OPR reconstruction (Fig. 4c). The tabulated scattering quotient[44] for the materials Al (aluminum, $f_q = -0.1$), SiO_2 (silicon dioxide $f_q = 2.0$), and Si_3N_4 (silicon nitride $f_q = 2.9$) at a photon energy of 92 eV is indicated by a black dotted line in (**b**), **c**. The semi-transparent areas indicate plus/minus one standard deviation from the mean scattering quotient in the corresponding areas. Using only the m-s method (**b**), the different materials cannot be identified reliably. For the combined m-s/OPR method (**c**), Al, SiO_2, and Si_3N_4 can be clearly distinguished. Energy-dispersive X-ray spectroscopy (EDX) measurements, for a region indicated by a black dashed box in (**a**), are shown in (**d**) for nitrogen and oxygen and in (**e**) for silicon and aluminum. The scale bar in (**a**), **d**, **e** has a size of 1 μm.

precision and referenced to an a priori known area (e.g., vacuum). Although the small, conducting structures of the integrated circuit are resolved in Fig. 4b, obvious imaging artifacts are present as well—for instance, the modulations in the vacuum region outside surrounding the specimen. We believe these artifacts can be attributed to small, remaining long-term drifts of the EUV beam on the mask. To reduce the influence of the drifts, we incorporated orthogonal-probe relaxation[27] (OPR) into the forward model of our analysis software[45]. However, because of decoherence effects (more details can be found in the "Materials and methods" section), the forward model in this experiment also required mixed-state (m-s) analysis[46]. We thus implemented a combined OPR and m-s analysis, as detailed in the "Materials and methods" section. The resulting reconstruction is shown in Fig. 4c and shows an improved image quality, as highlighted by the white inset at the right edge of the reconstruction field of view (Fig. 4d).

The material variety in the integrated circuit can be examined through the scattering quotient. We selected a region of interest (red dashed in Fig. 4c), which is shown in Fig. 5a. To quantitatively determine the contained materials, a histogram was evaluated for the areas indicated in Fig. 5a. Using the m-s method alone (Fig. 5b), we encountered difficulties in correctly classifying the contained materials. Using the m-s OPR method (Fig. 5c), we obtained well-separated peaks, which can be attributed to silicon nitride (region 1), silicon dioxide (regions 2 and 4), and aluminum (region 3). Our analysis was cross-validated by energy-dispersive X-ray spectroscopy (EDX). The nitrogen and oxygen traces are shown in Fig. 5d; silicon and aluminum are shown in Fig. 5e. The EDX measurements match well with the classification results from our scattering quotient analysis. However, there is one area (region 5) that deviates from the surrounding area. In this region, there appears to be surface contamination with carbon, since the scattering quotient

for this area increases (f_q (SiO_2) = 2.0, f_q (C) = 5.7). The contamination at this location can be traced back to a high-resolution transmission electron microscopy image, that was acquired after the lamella preparation, which led to a carbon build-up on the surface of the sample. Assuming pure carbon, the thickness of the contamination layer is determined to be 18 nm on each side. The lateral half-pitch resolution of our ptychography reconstruction was determined by an FRC to be 52 nm and is confirmed by resolved features with a half-pitch distance of 78 nm. More details on the estimation of the resolution can be found in the supplement.

Discussion

In this paper, we present material-specific high-resolution microscopy in the extreme ultraviolet using a table-top high-harmonic light source for the first time. By applying a high photon flux source, structured illumination, and active nanometer-scale stabilization, we achieved a half-pitch lateral resolution of 16 nm on a Siemens star test pattern which is only a factor of 4 larger than the resolution reached by state-of-the-art synchrotron facilities, where a half-pitch resolution down to 3.8 nm has been demonstrated[47]. So far a higher resolution using table-top EUV ptychography has been only reported for a periodic object using a knife-edge test[24].

By combining structured illumination with advanced data analysis, namely a combined mixed-state and orthogonal probe relaxation model, quantitative amplitude and phase imaging with high accuracy is demonstrated. The results were exploited for material-specific imaging of a complex integrated circuit, where a range of different materials have been identified including additional carbon contamination of the sample. This material classification is a novel functionality that significantly expands the capabilities of EUV imaging.

Since the 13.5 nm wavelength features low absorption, samples embedded in micrometer thick silicon environments can be investigated. The large penetration length enables high-resolution imaging and composition analysis of silicon-based nanomaterials, which are important for next-generation rechargeable batteries[3] or metamaterials[4]. Generally, ptychography in the EUV and soft X-ray range will benefit from the presented methods. In principle, the EUV photon energy can be adapted to resonances of other materials (up to 100 eV) by changing the wavelength selecting multilayer mirrors in the setup. For example, the M-edge resonance[48] of iron, nickel, or cobalt can be reached which, in combination with advanced polarization control, will enable imaging of extended magnetic structures (e.g., skyrmions) on a table-top.

Using the presented setup exotic beams with advanced functionalities can be realized, which was demonstrated by the generation of OAM beams of varying charges. This approach offers significantly higher flexibility and lowers experimental complexity compared to state-of-the-art table-top implementations[49–52]. Since OAM beams have already shown a wide variety of advantages in other spectral regions[53] we foresee a plethora of future applications of functional beams in the EUV, including actinic defect inspection via scatterometry with tailored beams[54] and OAM-induced dichroic spectroscopy[55].

Materials and methods

High-harmonic generation

To drive the high-harmonic process at 13.5 nm (compare Fig. 1), a fiber-based chirped-pulse amplifier operating at a central wavelength of 1030 nm is used. The amplifier consists of four coherently combined fibers that provide 1 mJ pulse energy and 250 fs pulse duration at a repetition rate of 75 kHz, which results in an average power of 75 W and power stability better than 0.5% rms. For efficient high-harmonic generation, the pulses are compressed by two hollow-core fibers to a pulse duration of <7 fs with a residual pulse energy of 400 μJ, resulting in an average power of 30 W. The few-cycle pulses are subsequently focused to a spot size of 75 μm ($1/e^2$) into a vacuum chamber. A gas jet with a diameter of 700 μm is placed near the focal spot and a backing pressure of 600 mbar argon is applied. To reduce the argon gas pressure in the vacuum chamber, a gas catch with a diameter of 3 mm directly opposite to the gas jet was installed which resulted in a pressure of 5×10^{-3} mbar in the vacuum chamber. The use of few-cycle IR pulses results in a broad EUV continuum reaching up to 12.4 nm wavelength (100 eV). In the next step, the high-power IR laser is separated from the EUV radiation. Four grazing incidence plates[56] separate the broadband EUV continuum from the IR-laser. The remaining IR-light is spectrally filtered by means of two 200 nm zirconium (Zr) foils. Sufficient pointing stability of the EUV beam was achieved by active stabilization of the driving IR laser beam yielding a pointing stability better than 1 μrad at the entrance of the vacuum chamber. The power stability of the EUV beam at 13.5 nm wavelength was characterized to be 0.8% rms. More details on the general setup of the HHG source can be found in earlier work[57].

Data acquisition and preprocessing

All samples were scanned using a Fermat spiral pattern[58]. The distance between adjacent positions was set to 1.0 μm for the Siemens star measurements and 0.7 μm for the integrated circuit. Since the integrated circuit has an elongated geometry, the scan grid was adjusted accordingly. The position of the mask and sample were measured by a laser interferometer (Picoscale, SmarAct GmbH) and fed back to the piezo-driver for active stabilization of the positioners (SLC 1740, SmarAct GmbH).

During the measurement, the camera (Andor iKon-L) was cooled down to $-60\,°C$ to minimize thermal noise. The CCD pixels were read-out at a rate of 1 MHz. In the Siemens star measurement, on-chip binning was set to 2×2, while for the integrated structure 1×1 binning was necessary due to a larger sample-mask distance. For each scan position, multiple diffraction patterns at varying exposure times were measured and merged into a single HDR image. The applied stitching method has been described in a previous publication[30]. A table with the most important measurement parameters can be found in the supplementary material. A background correction of the measured diffraction patterns was not necessary, because the vacuum chamber was completely dark. We note that the laser interferometer, employed for position stabilization, operates at a wavelength of 1550 nm at which the CCD is not sensitive.

Ptychography reconstruction

Initial reconstructions directly after the measurements were performed using the difference-map[59] implementation of the GPU-acceleration package of the PtyPy library[60]. The final reconstructions shown here were done using the ptylab framework[45], due to more specialized regulizers (e.g., TV) and models (e.g., mixed-state combined with orthogonal probe relaxation) that are available. For the reconstruction shown here, mPIE[61] combined with the mixed-state method[28] (m-s) are used. The mixed-state method[28] describes the measured far-field intensity I_j at position j as a sum over incoherent modes P_k.

$$I_j \sim \sum_k \left| \mathcal{F}\left[P_k(r) \cdot O(r - r_j) \right] \right|^2$$

Here $O(r)$ corresponds to the complex transmission of the object and $F[\cdot]$ to the Fourier transform operator modeling far-field diffraction. While HHG sources usually provide a high degree of spatial coherence[20], the m-s modes can also be employed to mitigate other sources of decoherence such as high-frequency sample vibrations[31], background, detector point-spread, or a finite spectral bandwidth[46]. The reconstructed probes shown in Fig. 2 are the dominant illumination mode in each data set, making up more than 50% of the power content. More details on the reconstructed m-s modes can be found in the supplement.

Beam pointing instability and scan stage position drifts that occur on a time scale longer than the exposure time of the camera, cannot be described by the m-s method. Instead, orthogonal probe relaxation (OPR)[27] allows to model probe variations $P_j(r)$ during the scan. This is achieved by relaxing the requirement for a stationary probe along the scan, which can be modeled by a truncated singular value decomposition over the set of probe estimates at each respective scan position j.

$$P_j(r) = \sum_i U_i(r) S_i V_{i,j}^*$$

Here $U_i(r)$ corresponds to the ith reconstructed eigen-probes, while $S_i V_{i,j}^*$ are expansion coefficients. Thus by allowing the probe modes to be drawn from a larger set of eigen-modes, probe variability can be modeled. We note that mixed states can model decoherence, but require beam stability, while OPR can only model fully coherent probes. For the reconstruction of the integrated circuit (Fig. 4b), the m-s method was combined with OPR, which accounts for both probe instability and decoherence effects throughout the measurement:

$$I_j \sim \sum_k \left| \mathcal{F}\left[\sum_i U_{i,k}(r) S_{i,k} V_{i,j,k}^* \cdot O(r - r_j) \right] \right|^2$$

The hybrid algorithm, which we refer to as *mixed-state orthogonal probe relaxation* (m-s OPR), solves for variable mixed states at each position. In contrast to a previous report[62], where the OPR method was applied to only the first mode of a mixed state model, we applied the OPR method to all mixed states.

Application of the m-s OPR method leads to fewer reconstruction artifacts, rendering image analysis more quantitative—a key to the reliable classification of materials based on the scattering quotient analysis reported here (compare Fig. 5). For the quantitative analysis of the integrated circuit, 4 mixed states, each comprising 4 OPR modes, resulted in a model containing a total of 16 probe modes (shown in the Supplementary Information).

Material characterization

Since the complex transmission function of the object reconstructed by ptychography provides both amplitude and phase information, the complex scattering quotient f_q can be calculated[43]. It is defined as the ratio of reconstructed phase $\phi(x, y)$ and the natural logarithm of the reconstructed amplitude $|O(x, y)|$:

$$f_q = \frac{\phi(x, y)}{\log(|O(x, y)|)} = \frac{\overline{f_1}}{\overline{f_2}} = \frac{\overline{\delta}}{\overline{\beta}}$$

here $\overline{\delta}$ and $\overline{\beta}$ correspond to the averaged refractive index along the projection direction of the measurement, where the refractive index of a material is given by $n = 1 - \delta - i\beta$. The advantage of the scattering quotient is that it is independent of the thickness of the sample. Since ptychography reconstructions are usually invariant under a global phase shift and amplitude scaling, the reconstructed

complex transmission must be referenced. In the integrated circuit data, the reconstructed amplitude is referenced to the surrounding vacuum region, which is indicated in Fig. 4a, c (see white box labeled "R"). Since for the m-s method (Fig. 4a)—and to a lower extent also for the m-s OPR method (Fig. 4c)—a slight phase curvature in the vacuum region was visible, a low-spatial frequency phase map was interpolated from the surrounding vacuum region and subtracted from the object reconstruction.

Ptychography enables the reconstruction of complex illumination (the probe). The numerical propagation of the reconstructed probe from the sample plane to the mask plane is achieved by the angular spectrum of plane waves method[63]. In short, the reconstructed probe $E(x, y, 0)$ propagated by a distance of Δz is given by:

$$E(x, y, \Delta z) = \mathcal{F}^{-1}\left\{ H(f_x, f_y, \Delta z) \cdot \mathcal{F}\{E(x, y, 0)\} \right\}$$

where F denotes the Fourier transform and $H(f_x, f_y, \Delta z)$ represents the transfer function of free space, given by:

$$H\left(f_x, f_y, \Delta z\right) = \exp\left(2\pi i \cdot \Delta z \sqrt{\frac{1}{\lambda^2} - f_x^2 - f_y^2} \right)$$

To estimate the mask to sample distance, the reconstructed probe was back-propagated to the location where the fabricated mask exhibited maximum edge sharpness.

Sample preparation and characterization

A commercially available SSD-drive (Samsung) has been disassembled and the die of one memory module has been exposed by wet chemical etching. In the next step, a lamella has been excavated by focussed ion beam milling, transferred (in situ) to a carrier structure (Omniprobe-grid), and further thinned to electron transparency using a ZEISS Auriga 40 focussed ion beam workstation. High-resolution reference analyses of the microstructure and composition were done using a FEI TITAN[3] G2 80-300 (S)TEM instrument operated at 300 kV equipped with a high-angle annular dark-field detector (HAADF, Fischione Model 3000) and an energy-dispersive X-ray spectrometry (EDXS) detector (four SDD detectors, FEI company).

Mask preparation

A $100 \times 100\ \mu m^2$ Si_3N_4 membrane with a thickness of 50 nm was used as a base for the mask fabrication. After coating it with 50 nm of copper (thermal evaporation) from the backside to support charge dissipation during the structuring process, a focused Ga^+ ion beam (FEI Helios G3 UC, 30 keV, 80 pA) was scanned over the Si_3N_4 surface to etch the desired aperture through the membrane and the copper layer. For this purpose, a black and white bitmap was used to define the structure consisting

of 1024×1024 pixels with a pitch of 12 nm by toggling the exposure time between 0 and 200 μs for black and white pixels, respectively. The writing was done within a single pass. Afterward, additional 220 nm of copper were deposited on the backside to achieve a final absorber thickness of 270 nm Cu + 50 nm Si_3N_4. Finally, the aperture shape was confirmed using STEM.

Author details
[1]Institute of Applied Physics, Abbe Center of Photonics, Friedrich-Schiller-Universität Jena, Albert-Einstein-Str. 15, 07745 Jena, Germany. [2]Helmholtz-Institute Jena, Fröbelstieg 3, 07743 Jena, Germany. [3]Leibniz Institute of Photonic Technology, Albert-Einstein-Straße 9, 07745 Jena, Germany. [4]Fraunhofer Institute for Microstructure of Materials and Systems IMWS, Walter-Hülse-Str. 1, 06120 Halle, Germany. [5]Fraunhofer Institute for Applied Optics and Precision Engineering IOF, Albert-Einstein-Str. 7, 07745 Jena, Germany

References
1. Wagner, C. & Harned, N. EUV lithography: lithography gets extreme. *Nat. Photonics* **4**, 24–26 (2010).
2. Priolo, F. et al. Silicon nanostructures for photonics and photovoltaics. *Nat. Nanotechnol.* **9**, 19–32 (2014).
3. Sun, Y. M., Liu, N. & Cui, Y. Promises and challenges of nanomaterials for lithium-based rechargeable batteries. *Nat. Energy* **1**, 16071 (2016).
4. Staude, I. & Schilling, J. Metamaterial-inspired silicon nanophotonics. *Nat. Photonics* **11**, 274–284 (2017).
5. Bogaerts, W. et al. Programmable photonic circuits. *Nature* **586**, 207–216 (2020).
6. Kauffman, R. L., Phillion, D. W. & Spitzer, R. C. X-ray production ~13 nm from laser-produced plasmas for projection x-ray lithography applications. *Appl. Opt.* **32**, 6897–6900 (1993).

7. Torretti, F. et al. Prominent radiative contributions from multiply-excited states in laser-produced tin plasma for nanolithography. *Nat. Commun.* **11**, 2334 (2020).

8. Barbee, T. W., Mrowka, S. & Hettrick, M. C. Molybdenum-silicon multilayer mirrors for the extreme ultraviolet. *Appl. Opt.* **24**, 883–886 (1985).

9. Chkhalo, N. I. et al. High-reflection Mo/Be/Si multilayers for EUV lithography. *Opt. Lett.* **42**, 5070–5073 (2017).

10. Miao, J. W. et al. Beyond crystallography: diffractive imaging using coherent X-ray light sources. *Science* **348**, 530–535 (2015).

11. Brizuela, F. et al. Microscopy of extreme ultraviolet lithography masks with 13.2 nm tabletop laser illumination. *Opt. Lett.* **34**, 271–273 (2009).

12. Wang, S. et al. Single-shot large field of view Fourier transform holography with a picosecond plasma-based soft X-ray laser. *Opt. Express* **28**, 35898–35909 (2020).

13. Brewer, C. A. et al. Single-shot extreme ultraviolet laser imaging of nanostructures with wavelength resolution. *Opt. Lett.* **33**, 518–520 (2008).

14. Kördel, M. et al. Laboratory water-window x-ray microscopy. *Optica* **7**, 658–674 (2020).

15. Pupeza, I. et al. Extreme-ultraviolet frequency combs for precision metrology and attosecond science. *Nat. Photonics* **15**, 175–186 (2021).

16. Popmintchev, T. et al. Bright coherent ultrahigh harmonics in the keV X-ray regime from mid-infrared femtosecond lasers. *Science* **336**, 1287–1291 (2012).

17. Klas, R. et al. Ultra-short-pulse high-average-power megahertz-repetition-rate coherent extreme-ultraviolet light source. *PhotoniX* **2**, 4 (2021).

18. Duarte, J. et al. Computed stereo lensless X-ray imaging. *Nat. Photonics* **13**, 449–453 (2019).

19. Zayko, S. et al. Ultrafast high-harmonic nanoscopy of magnetization dynamics. *Nat. Commun.* **12**, 6337 (2021).

20. Bartels, R. A. et al. Generation of spatially coherent light at extreme ultraviolet wavelengths. *Science* **297**, 376–378 (2002).

21. Thibault, P. et al. High-resolution scanning X-ray diffraction microscopy. *Science* **321**, 379–382 (2008).

22. Maiden, A. M. & Rodenburg, J. M. An improved ptychographical phase retrieval algorithm for diffractive imaging. *Ultramicroscopy* **109**, 1256–1262 (2009).

23. Seaberg, M. D. et al. Tabletop nanometer extreme ultraviolet imaging in an extended reflection mode using coherent Fresnel ptychography. *Optica* **1**, 39–44 (2014).

24. Gardner, D. F. et al. Subwavelength coherent imaging of periodic samples using a 13.5 nm tabletop high-harmonic light source. *Nat. Photonics* **11**, 259–263 (2017).

25. Baksh, P. D. et al. Quantitative and correlative extreme ultraviolet coherent imaging of mouse hippocampal neurons at high resolution. *Sci. Adv.* **6**, eaaz3025 (2020).

26. Tanksalvala, M. et al. Nondestructive, high-resolution, chemically specific 3D nanostructure characterization using phase-sensitive EUV imaging reflectometry. *Sci. Adv.* **7**, eabd9667 (2021).

27. Odstrcil, M. et al. Ptychographic coherent diffractive imaging with orthogonal probe relaxation. *Opt. Express* **24**, 8360–8369 (2016).

28. Thibault, P. & Menzel, A. Reconstructing state mixtures from diffraction measurements. *Nature* **494**, 68–71 (2013).

29. Grebing, C. et al. Kilowatt-average-power compression of millijoule pulses in a gas-filled multi-pass cell. *Opt. Lett.* **45**, 6250–6253 (2020).

30. Tadesse, G. K. et al. Wavelength-scale ptychographic coherent diffractive imaging using a high-order harmonic source. *Sci. Rep.* **9**, 1735 (2019).

31. Enders, B. *Development and Application of Decoherence Models in Ptychographic Diffraction Imaging*. PhD thesis, Technical University Munich (2016).

32. Maiden, A. M., Rodenburg, J. M. & Humphry, M. J. Optical ptychography: a practical implementation with useful resolution. *Opt. Lett.* **35**, 2585–2587 (2010).

33. Guizar-Sicairos, M. et al. Role of the illumination spatial-frequency spectrum for ptychography. *Phys. Rev. B* **86**, 100103 (2012).

34. Odstrčil, M. et al. Towards optimized illumination for high-resolution ptychography. *Opt. Express* **27**, 14981–14997 (2019).

35. Maiden, A. M. et al. Soft X-ray spectromicroscopy using ptychography with randomly phased illumination. *Nat. Commun.* **4**, 1669 (2013).

36. Baksh, P. D. et al. Wide-field broadband extreme ultraviolet transmission ptychography using a high-harmonic source. *Opt. Lett.* **41**, 1317–1320 (2016).

37. Loetgering, L. et al. Tailoring spatial entropy in extreme ultraviolet focused beams for multispectral ptychography. *Optica* **8**, 130–138 (2021).

38. Heckenberg, N. R. et al. Generation of optical phase singularities by computer-generated holograms. *Opt. Lett.* **17**, 221–223 (1992).

39. Fanciulli, M. et al. Observation of magnetic helicoidal dichroism with extreme ultraviolet light vortices. *Phys. Rev. Lett.* **128**, 077401 (2022).

40. Loetgering, L. et al. Generation and characterization of focused helical x-ray beams. *Sci. Adv.* **6**, eaax8836 (2020).

41. Vila-Comamala, J. et al. Characterization of high-resolution diffractive X-ray optics by ptychographic coherent diffractive imaging. *Opt. Express* **19**, 21333–21344 (2011).

42. van Heel, M. & Schatz, M. Fourier shell correlation threshold criteria. *J. Struct. Biol.* **151**, 250–262 (2005).

43. Jones, M. W. M. et al. Mapping biological composition through quantitative phase and absorption X-ray ptychography. *Sci. Rep.* **4**, 6796 (2014).

44. Henke, B. L., Gullikson, E. M. & Davis, J. C. X-ray interactions: photoabsorption, scattering, transmission, and reflection at $E = 50–30,000$ eV, $Z = 1–92$. *At. Data Nucl. Data Tables* **54**, 181–342 (1993).

45. Loetgering, L. et al. ptyLab: a cross-platform inverse modeling toolbox for conventional and Fourier ptychography. in *Proceedings of the OSA Imaging and Applied Optics Congress 2021* (Optical Society of America, 2021).

46. Yao, Y. et al. Broadband X-ray ptychography using multi-wavelength algorithm. *J. Synchrotron Radiat.* **28**, 309–317 (2021).

47. Shapiro, D. A. et al. An ultrahigh-resolution soft x-ray microscope for quantitative analysis of chemically heterogeneous nanomaterials. *Sci. Adv.* **6**, eabc4904 (2020).

48. Willems, F. et al. Magneto-optical functions at the 3p resonances of Fe, Co, and Ni: ab initio description and experiment. *Phys. Rev. Lett.* **122**, 217202 (2019).

49. Zürch, M. et al. Strong-field physics with singular light beams. *Nat. Phys.* **8**, 743–746 (2012).

50. Hernández-García, C. et al. Attosecond extreme ultraviolet vortices from high-order harmonic generation. *Phys. Rev. Lett.* **111**, 083602 (2013).

51. Kong, F. Q. et al. Controlling the orbital angular momentum of high harmonic vortices. *Nat. Commun.* **8**, 14970 (2017).

52. Gauthier, D. et al. Tunable orbital angular momentum in high-harmonic generation. *Nat. Commun.* **8**, 14971 (2017).

53. Shen, Y. J. et al. Optical vortices 30 years on: OAM manipulation from topological charge to multiple singularities. *Light: Sci. Appl.* **8**, 90 (2019).

54. Wang, B. et al. Coherent Fourier scatterometry using orbital angular momentum beams for defect detection. *Opt. Express* **29**, 3342–3358 (2021).

55. van Veenendaal, M. & McNulty, I. Prediction of strong dichroism induced by X rays carrying orbital momentum. *Phys. Rev. Lett.* **98**, 157401 (2007).

56. Pronin, O. et al. Ultrabroadband efficient intracavity XUV output coupler. *Opt. Express* **19**, 10232–10240 (2011).

57. Klas, R. et al. Generation of coherent broadband high photon flux continua in the XUV with a sub-two-cycle fiber laser. *Opt. Express* **28**, 6188–6196 (2020).

58. Huang, X. J. et al. Optimization of overlap uniformness for ptychography. *Opt. Express* **22**, 12634–12644 (2014).

59. Thibault, P. et al. Probe retrieval in ptychographic coherent diffractive imaging. *Ultramicroscopy* **109**, 338–343 (2009).

60. Enders, B. & Thibault, P. A computational framework for ptychographic reconstructions. *Proc. R. Soc. A: Math., Phys. Eng. Sci.* **472**, 20160640 (2016).

61. Maiden, A., Johnson, D. & Li, P. Further improvements to the ptychographical iterative engine. *Optica* **4**, 736–745 (2017).

62. Odstrčil, M. *Coherent Diffractive Imaging Using Table-top Sources*. PhD thesis, University of Southampton (2017).

63. Goodman, J. W. *Introduction to Fourier Optics* 3rd edn (Roberts & Company Publishers, 2005).